JTTEE5 16:651–660
DOI: 10.1007/s11666-007-9099-3
1059-9630/$19.00 © ASM International

Mechanical Characteristics of Al-Co-Ce Coatings Produced by the Cold Spray Process

E. Sansoucy, G.E. Kim, A.L. Moran, and B. Jodoin

(Submitted March 18, 2007; in revised form May 30, 2007)

Gas atomized feedstock particles of an Al-13Co-26Ce alloy system were sprayed using the Cold Spray deposition technique. The microstructures of the coatings produced are examined and the mechanical characteristics, in particular the bending fatigue and the bond strength, of the Al-Co-Ce coatings are reported. The results show that the Al-Co-Ce coatings improved the fatigue behavior of AA 2024-T3 specimens when compared to uncoated and Alclad specimens. During the bond strength tests, the bonding agent failed and no delamination of the coating from the substrate occurred. The microstructural features of the feedstock powder were also found in the coatings. It is suggested that the increase in the fatigue properties of the specimens can be attributed to the residual compressive stresses induced in the coatings and to the high adhesion strength of the coatings to the substrates.

Keywords aluminum alloy, Al-Co-Ce, bond strength, Cold Gas Dynamic Spray, fatigue, residual stresses

1. Introduction

Amorphous metals, also called metallic glasses, are characterized by their lack of defects such as grain boundaries and dislocations typically found in crystalline materials. The unique properties of these materials have pushed the development of this new class of alloys (Ref 1, 2). It has been shown that the areas of high local stresses and precipitation around the grain boundaries of crystalline materials promote the preferential nucleation of pits and lead to pitting corrosion (Ref 3). The absence of grain boundaries in aluminum-based amorphous alloys has resulted in improved mechanical properties as well as significant enhancements to corrosion resistance compared to their crystalline counterparts (Ref 4), such as a superior pitting resistance due to the limited number of pitting initiation sites (Ref 5). The addition of a late transition element such as cobalt, and a rare-earth element such as cerium, to an aluminum matrix, improves its glass formability and its corrosion protection abilities. When used as metallic coatings for aluminum components, an Al-Co-Ce alloy can act as a sacrificial anode and provide resistance to halide-induced pitting (Ref 6, 7). The presence of cobalt in solid solution is necessary to maintain the amorphicity of the Al-Co-Ce alloys. However, lower cobalt contents are desirable since the open circuit potential increases slightly in alloys with high cobalt content (Ref 8). The addition of cerium also improves the amorphicity of the alloy and offers sacrificial anodic protection by decreasing the open circuit potential (Ref 6).

Typical thermal spray (TS) processes, such as plasma and high velocity oxygen fuel spraying techniques have been successful in producing metallic amorphous coatings (Ref 9-12). The formation of the amorphous phase in the coatings is mainly attributed to the high cooling rates experienced by the molten droplets and splats associated with these processes. The amorphous content of the coating has been shown to depend on the spraying conditions. The critical cooling rate, for example, is influenced by factors such as the size of the sprayed particles (Ref 12) and their chemical composition (Ref 9). The particle size affects the heating and the acceleration of the particles in the high temperature gas flow and the resulting splats. In-flight particle oxidation alters the particle chemical composition within a molten droplet. It has been reported that the oxides produced during the process reduce the fraction of the elements required for the formation of a stable amorphous phase and hence change its associated critical cooling rate (Ref 9). Recrystallization of the amorphous phase can also occur during successive TS passes, causing localized reheating due to the deposition of molten

---

This article is an invited paper selected from presentations at the 2007 International Thermal Spray Conference and has been expanded from the original presentation. It is simultaneously published in *Global Coating Solutions, Proceedings of the 2007 International Thermal Spray Conference*, Beijing, China, May 14-16, 2007, Basil R. Marple, Margaret M. Hyland, Yuk-Chiu Lau, Chang-Jiu Li, Rogerio S. Lima, and Ghislain Montavon, Ed., ASM International, Materials Park, OH, 2007.

E. Sansoucy and **B. Jodoin**, Department of Mechanical Engineering, University of Ottawa, Ottawa, Ontario, Canada; **G.E. Kim**, Perpetual Technologies, Iles des Soeurs, Quebec, Canada; and **A.L. Moran**, Department of Mechanical Engineering, United States Naval Academy, Annapolis, MD, USA. Contact e-mail: sansoucy@genie.uottawa.ca.

droplets (Ref 10). The presence in the coating of the crystalline phase and chemical changes induced by the TS coating process, compared with the feedstock powder, represent inhomogeneities that modify the corrosion properties of the alloy. Crystalline materials are often susceptible to intergranular corrosion, where localized attacks occur at and adjacent to grain boundaries. The grain then disintegrates and may leave the underlying layer exposed to pitting corrosion. Intergranular corrosion can be resolved by replacing the crystalline phase by a non-crystalline or amorphous phase.

A different way to produce a fully amorphous coating and avoid chemical changes and recrystallization of the amorphous phase would consist of using amorphous feedstock powder particles and ensure that they undergo solid-state deformation in order to bond to the substrate and form the coating. Cold Gas Dynamic Spraying (CGDS) represents an emerging TS technology in which the process temperatures are kept well below the melting point of the sprayed material. Consequently, the feedstock powder particles experience no significant heating and in-flight melting or softening (Ref 13). This absence of significant heating of the feedstock powder eliminates the possibilities of grain growth and chemical reactions. In CGDS, the particles are injected in a supersonic flow and accelerated above the material's critical velocity (Ref 13). On impact with the substrate, the particles undergo intense plastic deformation and bond to the substrate to form a coating. The impact also disrupts the passivation layers, which provide intimate contact between the particles and the substrate for bonding to occur (Ref 13-15). Based on the microstructural examinations of coating produced by CGDS, no evidence of particle melting has been reported (Ref 14, 16), despite some localized melting predicted by theoretical models (Ref 17, 18). The laminar grain structure observed in CGDS is consistent with the absence of melting and grain growth during the particle deformation process and subsequent bonding (Ref 16, 19, 20). In CGDS, the microstructures of the powder and of the coating are similar. For example, nanocrystalline (Ref 21-23) and amorphous (Ref 24, 25) coatings have been successfully produced from nanocrystalline and amorphous feedstock powders, respectively. The CGDS process is capable of depositing a wide variety of aluminum alloys coatings (Ref 23, 26, 27).

In view of the aforementioned attributes of the CGDS process, it is foreseen that amorphous Al-Co-Ce coatings produced by this technique would constitute a promising application in the field of cathodic protection of aluminum structures. For example, such coatings could be used as cladding material to provide corrosion protection of the high-strength aluminum alloy on aircrafts skin structures (Ref 28). Although the corrosion behaviors of Al-Co-Ce alloys have been explored (Ref 6-8), their fatigue performance as a coating has not yet been investigated. The objective of this work is to demonstrate the feasibility of producing Al-Co-Ce coatings using a crystalline feedstock powder and the CGDS process. The mechanical properties of the coatings, such as the bond strength, fatigue behavior, hardness, and the microstructural features are examined.

2. Experimental Procedures

2.1 Powder Preparation

The Al-13Co-26Ce powder was prepared by gas atomization. The particles have a spherical morphology, as illustrated in Fig. 1. The particle size distribution, outlined in Fig. 2, indicates that the powder has an average diameter of 12 μm. About 90% of the particles have a size below 23 μm.

2.2 Coating Preparation

The aluminum alloy coatings were produced using the cold spray coating system developed at the University of Ottawa Cold Spray Laboratory. The system includes a spray chamber, a spray gun, a propellant gas heater, and a commercial powder feeder (Praxair Surface Technologies model 1264, Concord, NH, USA). The spray guns used in this study consist of converging-diverging nozzles specifically designed to allow aluminum feedstock powder to reach the high critical velocity of aluminum (Ref 16).

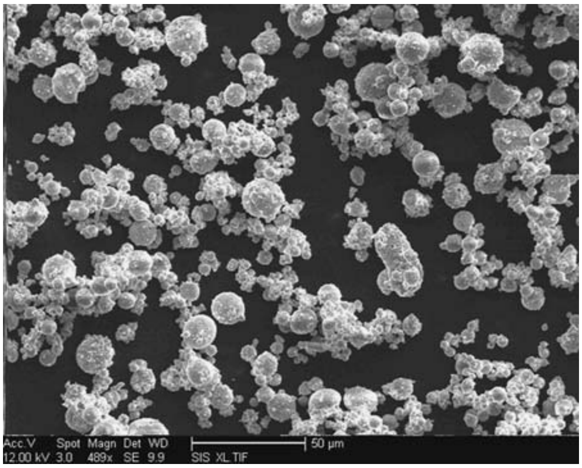

Fig. 1 Morphology of the Al-13Co-26Ce powder particles

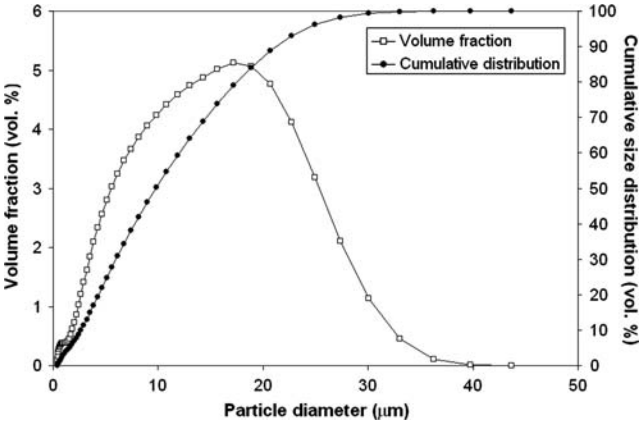

Fig. 2 Particle size distribution of the Al-13Co-26Ce feedstock powder

2.3 Spraying Parameters

Helium was chosen as the driving and feeding gas for its low molecular weight and to minimize the required gas stagnation temperature and pressure, since the set-up maximum injection pressure is limited by the powder feeder maximum operating pressure of 1100 kPa. At the same gas temperatures, helium yields greater velocities than nitrogen for a specified nozzle design (Ref 14). Tests were conducted at a gas stagnation pressure of 1.7 MPa and the gas stagnation temperature was set at two different values, 200 and 370 °C. The coatings were produced using single passes of the spray gun over grit-blasted aluminum substrates at a spraying distance of 10 mm.

Two axisymmetric nozzles with different exit-to-throat area ratios but identical converging-diverging length sections were considered to verify the effect of the area ratio on the coating quality. Nozzles with a throat diameter of 2 mm and with area ratios of 10 and 13 were used to produce the coatings. A nozzle with an area ratio of 13 and a constant traverse speed were used to examine the effects of the gas stagnation temperature and of the powder feed rate on the particle in-flight velocities and the resulting coatings.

2.4 Particle Velocity Measurements

Particle velocities were measured using a Cold Spray Meter (Tecnar Automation Ltd., St-Bruno, Québec, Canada), a laser in-flight diagnostic system. While a continuous laser illuminates a measurement volume, a dual-slit photomask captures the signal generated by individual particles passing in front of the sensor. The signal from the photosensor is then amplified, filtered, and analyzed. The in-flight diagnostic of each individual particle that crosses the measurement volume is performed by determining the time between two peaks of the particle signal. The particle velocities are then obtained by dividing the distance between the two-slits by the particle's flight time (Ref 29). In this study, the velocity measurements were taken at a location 10 mm from the spray gun exit. In order to avoid particle build-ups and rebounds that could obstruct the sensor field of view, the particle velocity measurements were performed without the presence of a substrate at the exit of the spray gun.

2.5 Coating Evaluation

The effects of the nozzle exit-to-throat area ratio, gas stagnation temperature, and powder feed rate are described from observations of the coatings using Scanning Electron Microscopy (SEM) images. Based on these microstructural examinations, optimum operating conditions were then selected and used to produce coatings to evaluate the fatigue behavior and the bond strength of the coatings.

The coating samples were sectioned and prepared for an SEM observation of the coating microstructure following standard metallographic techniques. Secondary electron and backscattered electron images of the coatings' cross-sections were used to evaluate the microstructural features such as thickness, porosity and interlamellar cracks. The area fraction of porosity was quantified using a gray scale delineation technique (Ref 30). Microhardness measurements were performed on mounted and polished samples using a Struers Duramin-2 tester (Ballerup, Denmark). The indentation measurements were conducted using a 500 g load (HV_{500g}) and a dwell time of 10 s. The microhardness values reported for each coating is the average of ten measurements. X-ray diffraction (XRD) measurements were carried out using a Philips X'Pert PW 1830 generator diffractometer with Cu Kα radiation at 50 steps per degree and a count time of two seconds per step.

The effects of the Al-Co-Ce coatings on the bending fatigue behavior of AA 2024-T3 were examined following the ASTM Standard B 593-96 (Ref 31). This test measures the ability of a material to withstand cyclic stress without developing cracks or other evidence of mechanical deterioration. The test specimens were supported in the same manner as a cantilevered beam at one end and were subjected to an alternating force at the other, as depicted in Fig. 3. The fatigue test specimen shown in Fig. 4 includes a triangular shape intended to produce a constant stress along the length of the test section of the specimen. This triangular region was grit-blasted and coated on one side only. Single passes, at 50% overlap, were used to cover this portion of the specimens with an Al-Co-Ce coating. In the current study, stress levels of 200, 275, and 350 MPa (30, 40, and 50 ksi, respectively) at a frequency of 30 Hz and a mean stress of zero were used to test the fatigue behavior of the coated samples. Two to three

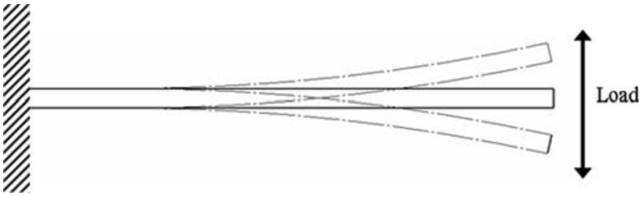

Fig. 3 Cantilevered beam subjected to an alternating load

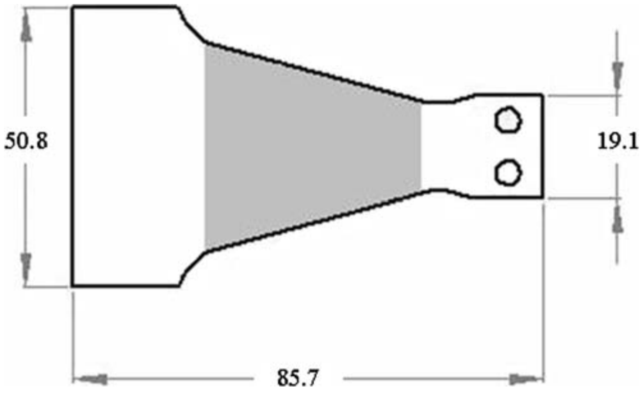

Fig. 4 Bending fatigue strength specimen. The gray region corresponds to the coated area. Dimensions are in mm

specimens were tested at each stress level. The number of cycles was automatically recorded until complete sample failure, characterized by the separation of the specimen into two pieces. The fatigue behavior of the coated test samples was then compared to uncoated AA 2024-T3 and Alclad specimens.

Bond strength evaluations were conducted using the ASTM Standard C 633-01 (Ref 32). Coatings were produced on grit-blasted standard test samples having a 25.4 mm diameter and an overall length of 38.1 mm. Several passes were carried out to cover the entire surface of the sample. The top portion of the coatings were machined flat and glued to an uncoated test sample, using an adhesive (Master Bond EP-15, Hackensack, NJ, USA). The assembled parts were cured at 170 °C for 90 min in a V block device that ensures proper alignment. Before testing the coatings, the bonding agent was tested separately on uncoated test samples, and failed on average at 82 MPa, which conforms to the product specifications.

3. Results and Discussion

3.1 Parametric Study

A parametric study of three spraying parameters was first undertaken to examine the effects of the nozzle exit-to-throat area ratio, the gas stagnation temperature, and the powder feed rate on the coating microstructural features. This parametric study was performed to obtain optimum spraying conditions that will be used to evaluate the fatigue behavior and bond strength of Al-Co-Ce coatings.

3.1.1 Effect of the Nozzle Exit-to-Throat Area Ratio. Cross-sectional SEM images in Fig. 5 depict the Al-Co-Ce coating produced by CGDS with nozzles having different exit-to-throat area ratios but identical lengths. The gas stagnation temperature and the powder feed rate were set at 200 °C and 6 g/min, respectively. Both coatings exhibit levels of particle plastic deformation suggesting that the particles were accelerated beyond the alloy critical velocity by both nozzles. Increasing the nozzle area ratio reduced the coatings porosity from 2% to 0.5% while the coating thickness remained approximately constant at 200 μm. No significant changes in the coatings' microhardness were observed. Microhardness values of 226 ± 12 HV_{500g} and 229 ± 11 HV_{500g} were obtained for the coatings produced with the nozzle having an area ratio of 10 and 13, respectively.

Under similar conditions, the gas dynamics theory predicts that the gas undergoes a greater expansion in a nozzle with a greater exit-to-throat area ratio and thus higher gas velocities are expected in the latter nozzle (Ref 33). This behavior has been observed by monitoring the gas static pressure in nozzles along their length using static pressure taps (Ref 34). It was observed that the gas static pressure along the nozzle axis decreases more in the case of a nozzle with a greater exit-to-throat area ratio, confirming that the gas is expanded to a larger extent in this nozzle. The results from a validated two-dimensional numerical analysis of the nozzles indicate that increasing the nozzle exit-to-throat area ratio by 30% increases the gas velocity by approximately 6% (Ref 35). According to the model, this increase in the nozzle exit-to-throat increased the nozzle exit Mach number from 2.25 to 2.63. However, a greater expansion in a nozzle causes a larger drop of the gas static temperature, which reduces the local gas speed of sound, thus minimizing the increase of velocity of the gas despite a higher local Mach number (Ref 33). The numerical results have also shown that a larger exit-to-throat area ratio produces a slightly higher gas velocity at every radial position inside the nozzle (Ref 16, 35). The particle velocity measurements, shown in Fig. 6, demonstrate that increasing the nozzle exit-to-throat area ratio by 30% changed the particle velocity from 530 ± 110 to 549 ± 93 m/s. It is important to note that these velocity measurements were taken along the centerline of the nozzle and do not reflect the radial distribution of the particle velocity but represent the average particle velocity at the nozzle centerline. Based on the numerical results, the nozzle with a larger exit-to-throat area ratio generated a broader particle velocity profile due to the reduced area occupied by the boundary layer.

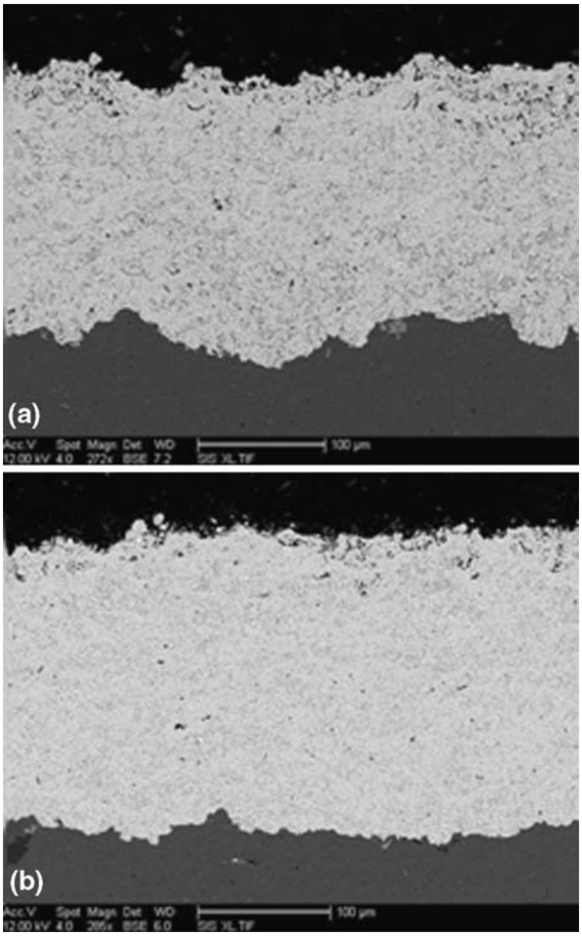

Fig. 5 SEM images of the cross-section of CGDS Al-Co-Ce coatings for nozzle exit-to-throat area ratios of (a) 10 and (b) 13

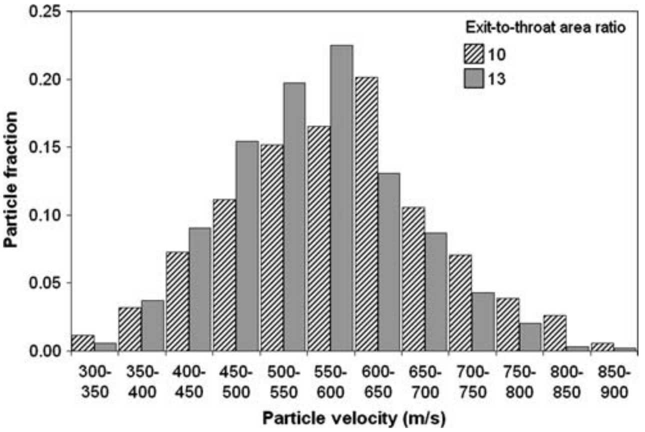

Fig. 6 Histograms of the Al-Co-Ce particle velocities for nozzle exit-to-throat area ratios of 10 and 13

The different microstructural features found in the coatings of Fig. 5 may be the result of a change in the profile of the particle velocity due to an increase of the nozzle area ratio. In addition, the velocity measurements were performed without a substrate at the nozzle exit. The presence of a perturbation such as a substrate generates abrupt changes in the flow properties through shock waves. It is also envisioned that the structure and the strength of the compression and expansion waves, which are dependant on the nozzle, influence the velocity of the fine particles (average diameter of 12 μm) (Ref 34). Flow visualization of the CGDS process has demonstrated that shock waves, entrainment of the ambient air, and jet flapping influence the flow pattern and the velocity of the feedstock powder particles (Ref 21). The difference in the average particle impact velocity is possibly greater than what is suggested by the velocity measurements performed without the presence of a substrate. Particle velocity measurement with a substrate could not be performed adequately because the substrate reduced the space required for the diagnostic system and caused poor particle illumination. Particle rebounds that obstructed the sensor field of view and reflections of the laser beam off the substrate and the nozzle are factors that affected the measurements with a substrate.

An increase of the particle velocities enhances the plastic deformation of the particles on impact and reduces the porosity of the coating by allowing the particles to conform to the existing shape of the coating. A close examination of the coating produced with a nozzle area ratio of 10 reveals particles deformed to a lesser degree with voids and pores surrounding these particles than the coating produced with the larger nozzle area ratio. Densification of the previously deposited layers of material due to the impact of impinging particles, similar to what is found in shot peening, was also observed in both coatings. This is confirmed by the observation that the top layers of the coatings are more porous than its bottom layers. The top layers consist of deformed particles that have not been exposed to the impingement of other incoming particles. Accordingly, the porosity of those regions of the coatings is greater than elsewhere in the coatings. The reduction of voids and pores in the coating produced with the larger nozzle area ratio is then attributed to the amount of compaction. The measured increase in the particle impact velocity not only enhances the plastic deformation of the particles on impact, but also intensifies the continuous compaction of the previously deposited layers of material by the incoming particles.

The fact that the coating thickness is not affected by the increase of the nozzle area ratio suggests that the latter did not influence the process deposition efficiency since the same powder feed rate was used for both nozzles. The interfaces free of defects between the substrates and the coatings indicate that a sufficient particle impact velocity was reached for deposition to produce an intimate bond at the coating-substrate interface. Although a slight enhancement of the particle plastic deformation was observed in the coating produced with the nozzle area ratio of 13, the microhardness measurements were not affected by the level of plastic deformation or additional work hardening resulting from the spraying process.

3.1.2 Effect of the Gas Stagnation Temperature. Scanning Electron Microscopy images of Al-Co-Ce coatings produced at stagnation temperatures of 200 and 370 °C are shown in Fig. 7. The larger nozzle area ratio was used since the coatings resulting from the previous nozzle area ratio study had a lower porosity and more visible particle plastic deformation. A powder feed rate of 6 g/min was also used to produce these coatings. Both coatings display substrate-coating interfaces free of defects and cracks and comparable porosity levels of less than 0.5%. The coating thickness was increased from 200 to 400 μm by raising the gas stagnation temperature. A higher gas stagnation temperature results in a higher static gas temperature throughout the nozzle. Since the gas velocity at any location in the nozzle is a function of the local Mach number (determined by the nozzle geometry) and the local speed of sound (which is a function of the gas static temperature), increasing the gas stagnation temperature increases the gas velocity throughout the nozzle (Ref 33). This, in turn, is likely to accelerate the particles to higher velocities due to the enhanced momentum transfer caused by the higher gas velocity. The increased coating thickness indicates that a larger portion of the particle distribution has reached the required velocity to plastically deform on impact. The histograms of the measured particle velocity obtained for gas stagnation temperature of 200 and 370 °C are presented in Fig. 8. Increasing the gas stagnation temperature from 200 to 370 °C increased the average particle velocities from 549 ± 93 to 599 ± 103 m/s. Despite an increase of the average particle velocity, the degree of the particle plastic deformation in both coatings is comparable since the interfaces of undeformed particles are difficult to outline. These results suggest that particle velocities above 550 m/s seem to undergo similar levels of plastic deformation to form dense and defect-free coatings.

At both gas stagnation temperatures, the top layers consist of deformed particles that were not exposed to the impingement of particles throughout the spaying process.

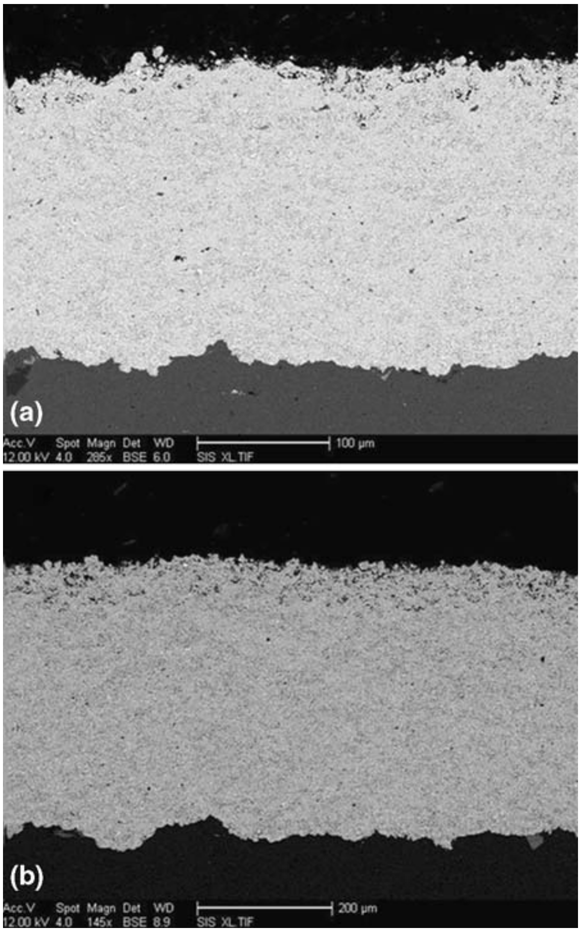

Fig. 7 SEM images (at different magnifications) of the cross-section of CGDS Al-Co-Ce coatings produced at (a) 200 °C and (b) 370 °C

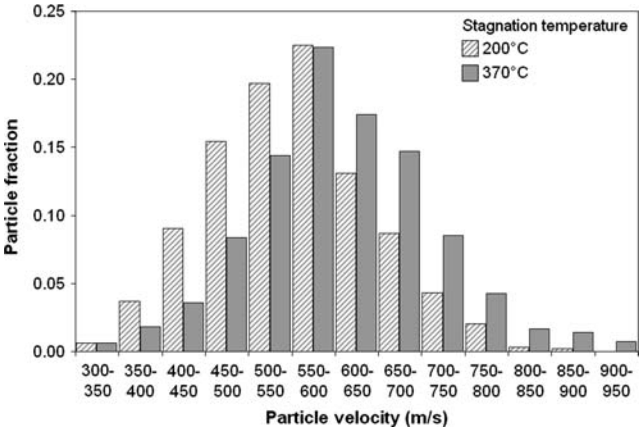

Fig. 8 Histograms of the Al-Co-Ce particle velocities at gas stagnation temperatures of 200 °C and 370 °C

The reduction of porosity in the underlying layers of deposited material was the result of a gradual compaction caused by the repeated impact of incoming particles on

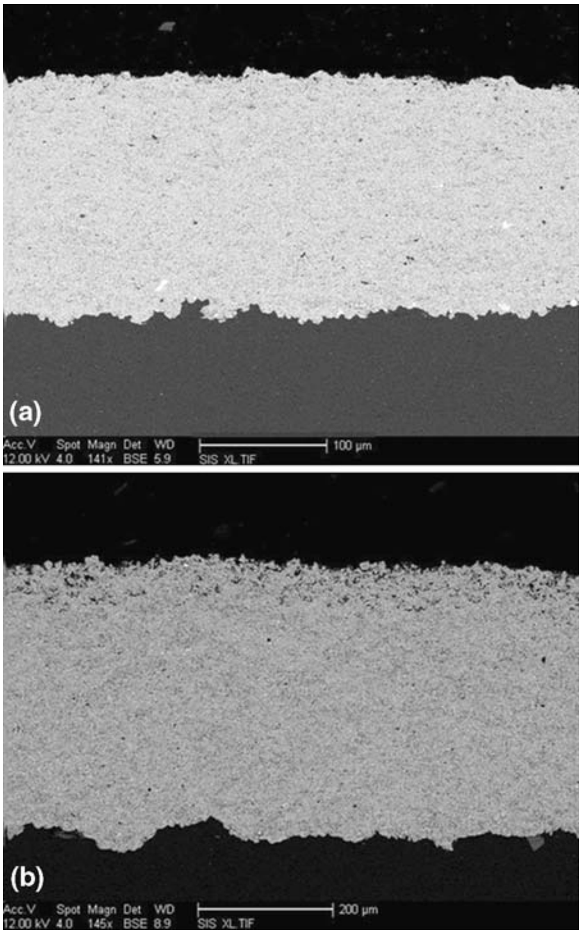

Fig. 9 SEM images (at different magnifications) of the cross-section of CGDS Al-Co-Ce coatings produced with a gas stagnation temperature of 370 °C and at feed rates of (a) 3 g/min and (b) 6 g/min

the coating. No apparent reduction of the porosity and no significant change in the microhardness were noticed by varying the gas stagnation temperature. Microhardness values of 229 ± 11 HV_{500g} and 231 ± 10 HV_{500g} were obtained for the coatings produced at 200 and 370 °C, respectively.

3.1.3 Effect of the Powder Feed Rate. The effect of the powder feed rate was evaluated on coatings produced with a nozzle with an area ratio of 13 and a gas stagnation temperature of 370 °C. Changing the feed rate of the Al-Co-Ce powder initiated a significant effect on the resulting coating thickness, as shown in Fig. 9. The coating thickness decreased from 400 to 200 μm by decreasing the powder feed rate from 6 to 3 g/min. At both feed rates, the coatings demonstrated dense and compact microstructures with substrate-coating interfaces free of cracks. The porosity in both coatings was evaluated at less than 0.5%. The similarities between the coatings suggest a comparable plastic deformation at both feed rates. A particle loading effect on the main flow in which the particle velocities are reduced below their critical velocity was not experienced. Particle loading occurs when the gas flow becomes saturated with powder particles. As a result, the momentum transfer between the gas flow and the particles is not sufficient and the particles are not accelerated above the required critical velocity. The measured particle velocity histograms of Fig. 10 show that the particle velocities were not affected by the powder feed rate. Doubling the powder feed rate from 3 to 6 g/min changed the particle velocity from 605 ± 104 to 599 ± 103 m/s and the microhardness measurements from 229 ± 13 HV_{500g} to 231 ± 10 HV_{500g}.

It is interesting to note that increasing the powder feed rate produced a similar effect than raising the gas stagnation temperature of the process. Similar values of thickness, porosity, and hardness were measured for the coatings produced at 6 g/min and 200 °C and at 3 g/min and 370 °C with the nozzle with an area ratio of 13. An increase in the process gas stagnation temperature only accelerated more particles above the critical velocity without affecting the microstructure of the coating.

3.1.4 Results of the Parametric Study. The results of the parametric study are summarized in Table 1. Based on these results, it was possible to select optimized parameters to conduct a comprehensive analysis of the mechanical properties of Al-Co-Ce coatings. A dense coating with a minimum thickness of 200 μm was required for the purpose of using Al-Co-Ce coatings as cladding material. The nozzle with an area ratio of 13, with a gas stagnation temperature of 200 °C, and a powder feed rate of 6 g/min were found to yield coatings that met the requirements. However, the top layers of these coatings were less dense than their bottom portion. The coatings produced with the nozzle with an area ratio of 13, with a gas stagnation temperature of 370 °C and a powder feed rate of 3 g/min were very dense and thick enough for the application. However, nozzle clogging has been encountered for prolonged spraying at this stagnation temperature and powder feed rate when using aluminum alloy powders, such as Al-5083, Al-2618, and Al-12Si. The feedstock particles may be entrained in the slow moving gas in the boundary layer and stick to the nozzle wall. The accumulation of these particles could obstruct the passage of the process gas and reduce the particle velocities. It was then decided to reduce the gas stagnation temperature to an intermediate value of 320 °C and to set the powder feed rate at 4 g/min in order to minimize the possibility of nozzle clogging.

3.2 Mechanical Properties Evaluation

The experimental results of the bending fatigue tests for the bare, Alclad coated and Al-Co-Ce coated specimens are presented in Fig. 11. At all three stress levels, the specimens with CGDS deposited Al-Co-Ce outperformed the bare and the Alclad coated specimens. At a stress of 350 MPa, the Alclad and the Al-Co-Ce coated specimens failed at about the same number of cycles. However, as the stress amplitude decreases, the Al-Co-Ce coatings significantly improve the fatigue performance of the substrates. At 200 MPa, the Al-Co-Ce coatings outlasted the bare and the Alclad specimens by over an order of magnitude.

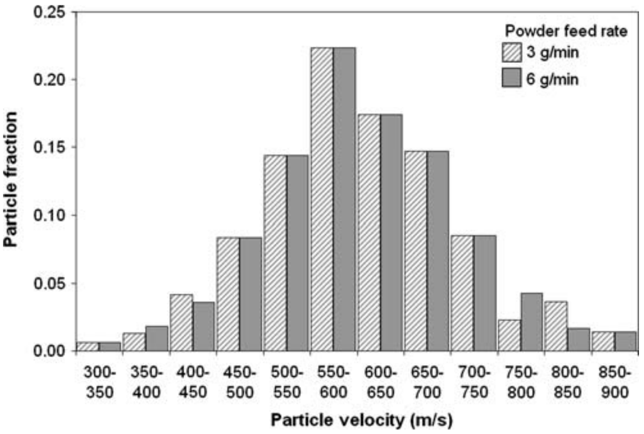

Fig. 10 Histograms of the Al-Co-Ce particle velocities at powder feed rates of 3 and 6 g/min and at a gas stagnation temperature of 370 °C

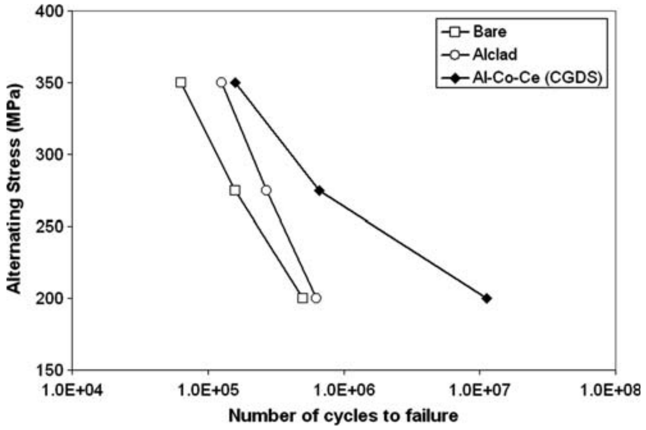

Fig. 11 Mean number of cycles prior to failure as a function of the alternating stress obtained from the bending fatigue tests of the bare, Alclad, and CGDS Al-Co-Ce coating on AA 2024-T3 specimens

Table 1 Results of the parametric study

Nozzle exit-to-throat area ratio	Gas stagnation temperature, °C	Powder feed rate, g/min	Particle velocity, m/s	Thickness, μm	Porosity, %	Microhardness, HV_{500g}
10	200	6	530 ± 110	200	2	226 ± 12
13	200	6	549 ± 93	200	0.5	229 ± 11
13	370	6	599 ± 103	400	0.5	231 ± 10
13	370	3	605 ± 104	200	0.5	229 ± 13

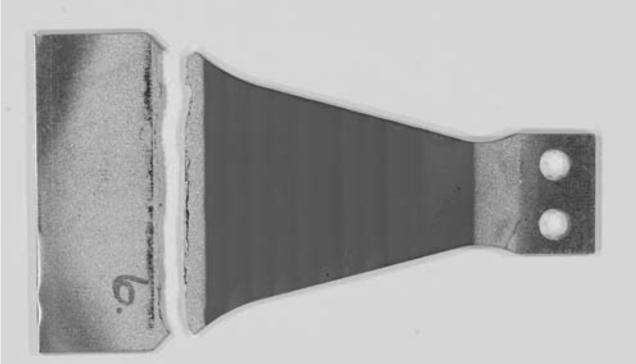

Fig. 12 Photograph of a bending fatigue specimen with an Al-Co-Ce coating after the test. Failure occurred outside the coated area

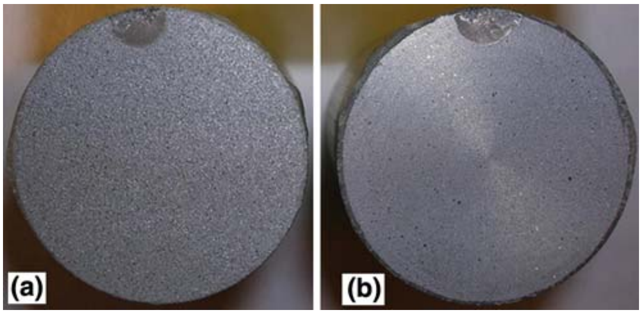

Fig. 13 Photograph of the bond strength specimens with (a) the bonding agent and (b) the remainder of the Al-Co-Ce coating after the test

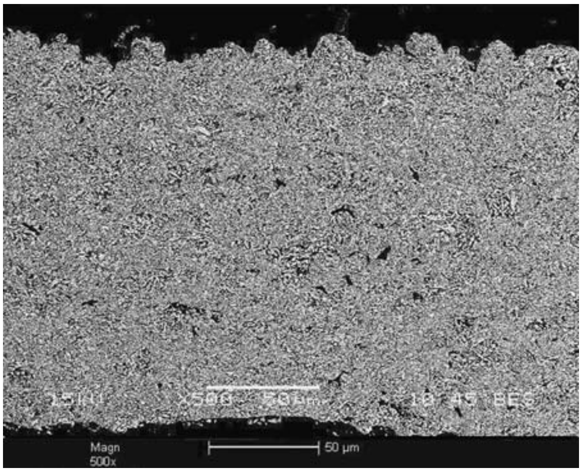

Fig. 14 SEM image of the cross-section of an Al-Co-Ce coating produced on a fatigue strength specimen

The fatigue curve for the coated samples indicates that the Al-Co-Ce coatings give rise to a significant increase in fatigue properties of the coated substrates in comparison with the uncoated substrates at all stress levels. It is interesting to note that during the tests, delamination of the Al-Co-Ce coatings from their substrates did not take place and failure occurred outside the coated area, as shown in Fig. 12. The Al-Co-Ce coatings remained completely attached to the substrates for all tests.

The adhesion level of the Al-Co-Ce coatings was evaluated through bond strength tests. The coatings produced on standard adhesion strength specimens failed at an average strength 61 ± 4 MPa. The failures occurred partly in the coating (cohesive) and partly in the bonding agent. Figure 13 illustrates the mixed failure mode between the glue and the coating. Consequently, the adhesive strength of the Al-Co-Ce coatings is larger than the reported value since the coating remained attached to the coated specimen. These bond strength results for the Al-Co-Ce coatings are significantly greater that typical values obtained for CGDS coatings. Cohesive strengths of 33 and 35 MPa (Ref 36) and of 25–49 MPa (Ref 19) have previously been obtained by performing cohesive strength tests on pure aluminum coatings removed from their substrates. Adhesion strength of 46 MPa for Al-5083 CGDS coatings, where the coating completely detaches from the substrate, have been reported (Ref 26).

The fatigue results can be rationalized on the basis of two important factors: the existence of residual compressive stresses, and the high adhesion of the coatings to the substrate. In CGDS, compressive stresses are induced in the coatings. The high velocity impacts of particles cause plastic deformation of the underlying layers and generate compressive residual stresses (Ref 37). These stresses can play a significant role in improving the fatigue behavior of materials by delaying crack initiation and propagation. However, the stresses that exist within a cold spray coating are only beneficial if the coating remains attached to the substrate. Hence, the appropriate adhesion of the coatings to the substrates also contributed in improving the fatigue properties of the AA 2024-T3 substrates.

3.3 Coating Microstructure

The cross-section of the coated region of a tested fatigue specimen is shown in Fig. 14. The coating remained well adhered to the substrate during fatigue testing, which confirms the absence of any delamination of the coating from the substrate. The coating remained structurally intact as neither damages nor cracks as a result of the fatigue test were found in the coating. Figure 15 shows the XRD patterns for the Al-13Co-26Ce powder and a CGDS coating. These results demonstrate that no microstructural changes occurred during the spraying process. The observed peak broadening in the XRD pattern of the coating was initiated by the residual stresses that were produced during the spraying process. Residual stresses may be classified into two categories based on the volume over which the stresses are homogeneous (Ref 38). Macrostresses are approximately constant over a large number of grains and initiate a line shift to a different angle of the diffraction pattern. The stresses that are uniform over distances of the order of a few grains are called microstresses. Microstresses cause diffraction line broadening due to changes in the range of the average distance

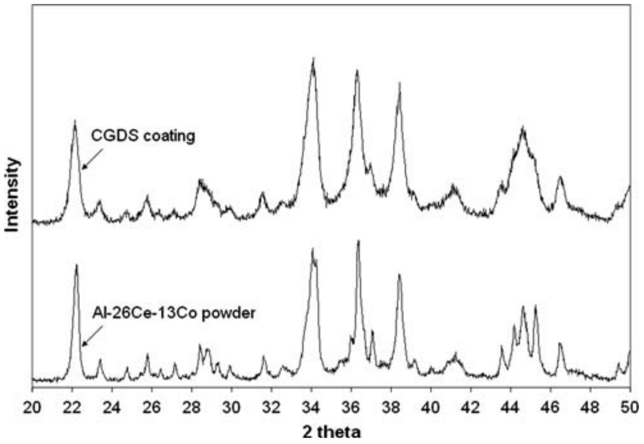

Fig. 15 XRD patterns for the Al-13Co-26Ce powder and a CGDS coating

separating the plane in a crystal for the same diffraction angle. Compressive stresses reduce the spacing which widens the diffraction profile, whereas tensile stresses contract the pattern as a result of larger spacing. Dislocations, defects, vacancies, and contractions are sources of microstresses (Ref 39). The extensive particle plastic deformation and the repeated impact of rapidly moving particles throughout the deposition process may have generated the compressive microstresses detected at the surface of the coating by reducing the distances between planes. The XRD pattern of the coating shows no evidence of macrostresses. However, the subsequent layers of material beneath the surface may reveal the presence of macrostresses that would contribute to the beneficial residual stresses induced in the coating.

4. Conclusions

The feasibility of producing coatings from an Al-Co-Ce alloy system by the CGDS process has been demonstrated. The mechanical properties of the deposits were evaluated based on the fatigue behavior, bond strength, and hardness. The porosity within the coatings was obtained from a microstructural analysis.

The Al-Co-Ce coatings give rise to a substantial increase in the fatigue properties in comparison with the uncoated and the Alclad coated substrates. It was proposed that any crack propagation in the coating was hindered by the residual compressive stresses contained in the coating. In addition, an excellent adhesion prevented delamination of the coatings from the substrates. Bond strength tests of Al-Co-Ce coatings confirmed their high degree of bonding to substrates. During these tests, fracture occurred within the coating and within the adhesive and not at the substrate-coating interface. A microstructural examination of a tested fatigue sample indicated that the coatings remained structurally intact, which was supported by the absence of any damages in the coating. Verified by an XRD analysis, the microstructure of the powder was preserved in the coating. Consequently, it is expected that the use of an amorphous Al-Co-Ce powder to produce coatings on aluminum alloys may be achievable and would provide improved corrosion resistance as well as increased fatigue resistance of the coated component.

Acknowledgment

The authors wish to acknowledge the financial support of the Natural Sciences and Engineering Research Council of Canada (NSERC).

References

1. A. Inoue, Stabilization of Metallic Supercooled Liquid and Bulk Amorphous Alloys, *Acta Mater.*, 2000, **48**, p 279-306
2. W.L. Johnson, Bulk Amorphous Metal—An Emerging Engineering Material, *JOM*, 2002, **54**(3), p 40-43
3. K. Urushino and K. Sugimoto, Stress-Corrosion Cracking of Aged Al-Cu-Mg Alloys in NaCl Solution, *Cor. Sci.*, 1979, **19**, p 225-236
4. F. Sanchette, A. Billard, and C. Frantz, Mechanically Reinforced and Corrosion-Resistant Sputtered Amorphous Aluminum Alloy Coatings, *Surf. Coat. Technol.*, 1998, **98**, p 1162-1168
5. J.E. Sweitzer, G.J. Shiflet, and J.R. Scully, Localized Corrosion of $Al_{90}Fe_5Gd_5$ and $Al_{87}Ni_{8.7}Y_{4.3}$ Alloys in the Amorphous, Nanocrystalline and Crystalline States: Resistance to Micrometer-Scale Pit Formation, *Electrochem. Acta*, 2003, **48**, p 1223-1234
6. J.G. Hoekstra, S.B. Qadri, J.R. Scully, and J.M. Fitz-Gerald, Laser Surface Modification of a Crystalline Al-Co-Ce Alloy for Enhanced Corrosion Resistance, *Adv. Eng. Mat.*, 2005, **7**(9), p 805-809
7. M.E. Goldman, N. Ünlü, G.J. Shifflet, and J.R. Scully, Selected Corrosion Properties of a Novel Amorphous Al-Co-Ce Alloy System, *Electrochem. Solid-State Lett.*, 2005, **8**(2), p B1-B5
8. F.J. Presuel-Moreno, M.E. Goldman, R.G. Kelly, and J.R. Scully, Electrochemical Sacrificial Cathodic Prevention Provided by an Al-Co-Ce Metal Coating Coupled to AA2024-T3, *J. Electrochem. Soc.*, 2005, **8**, p B302-B310
9. H. Choi, S. Lee, B. Kim, H. Jo, and C. Lee, Effect of In-Flight Particle Oxidation on the Phase Evolution of HVOF NiTiZrSiSn Bulk Amorphous Coating, *J. Mater. Sci.*, 2005, **40**, p 6121-6126
10. Y. Wu, P. Lin, G. Xie, J. Hu, and M. Cao, Formation of Amorphous and Nanocrystalline Phases in High Velocity Oxy-Fuel Thermally Sprayed a Fe-Cr-Si-B-Mn Alloy, *Mater Sci. Eng. A*, 2006, **430**, p 34-39
11. J. Jayaraj, D.J. Sordelet, D.H. Kim, Y.C. Kim, and E. Fleury, Corrosion Behaviour of Ni-Zr-Ti-Si-Sn Amorphous Plasma Spray Coating, *Cor. Sci.*, 2006, **48**, p 950-964
12. P. Rohan, S.Bouaricha, J.-G. Legoux, C. Moreau, P. Citbor, S. Nourouzi, and A. Vardelle, Deposition of Amorphous Metallic Coatings by Thermal Spraying, *Thermal Spray 2004: Advances in Technology and Application*, May 10-12, 2004 (Osaka, Japan), ASM International, 2004, p 382-389
13. A.P. Alkhimov, A.N. Papyrin, and V.F. Kosarev, "Gas Dynamic Spraying Method for Applying a Coating," U.S. Patent 5,302,414, April 12, 1994
14. R.C. Dykhuizen and M.F. Smith, Gas Dynamics Principles of Cold Spray, *J. Therm. Spray Technol.*, 1998, **7**(2), p 205-212
15. R.C. Dykhuizen, M.F. Smith, D.L. Gilmore, R.A. Neiser, X. Jiang, and S. Sampath, Impact of High Velocity Cold Gas Spray Particles, *J. Therm. Spray Technol.*, 1999, **8**(4), p 559-564
16. L. Ajdelsztajn, B. Jodoin, G.E. Kim, J.M. Schoeneug, and J. Mondoux, Cold Spray Deposition of Nanocrystalline Aluminum Alloys, *Met. And Mat. Trans. A*, 2005, **36A**, p 657-666
17. H. Assadi, F. Gärtner, T. Stoltenhoff, and H. Kreye, Bonding Mechanism in Cold Gas Spraying, *Acta Mater.*, 2003, **51**, p 4379-4394

18. M. Grujicic, C.L. Zhao, W.S. DeRosset, and D. Helfritch, Adiabatic Shear Instability Based Mechanism for Particles/Substrate Bonding in Cold-Gas Dynamic-Spray Process, *Mat. Des.*, 2004, **25**, p 681-688
19. T.H. Van Steenkiste, J.R. Smith, and R.E. Teets, Aluminum Coatings Via Kinetic Spray with Relatively Large Powder Particles, *Surf. Coat. Technol.*, 2002, **154**, p 237-252
20. A.O. Tokarev, Structure of Aluminum Powder Coatings Prepared by Cold Gas Dynamic Spraying, *Met. Sci. Heat Treat.*, 1996, **38**(3-4), p 136-139
21. V. Shukla, G.S. Elliot, and B.H. Kear, Nanopowder Deposition by Supersonic Rectangular Jet Impingement, *J. Therm. Spray Technol.*, 2000, **9**(3), p 394-398
22. R.S. Lima, J. Karthikeyan, C.M. Kay, J. Lindermann, and C.C. Berndt, Microstructural Characteristics of Cold-Sprayed Nanostructured WC-Co Coatings, *Thin Solid Films*, 2002, **416**, p 129-135
23. L. Ajdelsztajn, A. Zúniga, B. Jodoin, and E.J. Lavernia, Cold-Spray Processing of a Nanocrystalline Al-Cu-Mg-Fe-Ni Alloy with Sc, *J. Therm. Spray Technol.*, 2006, **15**(2), p 184-190
24. L. Ajdelsztajn, B. Jodoin, P. Richer, E. Sansoucy, and E.J. Lavernia, Cold Gas Dynamic Spraying of Iron-Base Amorphous Alloy, *J. Therm. Spray Technol.*, 2006, **15**(4), p 495-500
25. S. Yoon, H.J. Kim, and C. Lee, Deposition Behavior of Bulk Amorphous NiTiZrSiSn According to the Kinetic and Thermal Energy Levels in the Kinetic Spraying Process, *Surf. Coat. Technol.*, 2006, **200**, p 6022-6029
26. E. Sansoucy, B. Jodoin, P. Richer, and L. Ajdelsztajn, Effect of Spraying Parameters on the Microstructure and Bond Strength of Cold Spray Aluminum Alloy Coatings, *Thermal Spray 2006: Building on 100 Years of Success*, ASM International, May 15-18, 2006 (Seattle, WA, USA), B.R. Marple, M.M. Hyland, Y.-C. Lau, R.S. Lima, and J. Voyer, Ed. (Materials Park, OH), ASM International, 2006, 396 p
27. L. Zhao, K. Bobzin, D. He, J. Zwick, F. Ernst, and E. Lugscheider, Deposition of Aluminum Alloy Al12Si by Cold Spraying, *Adv. Eng. Mater.*, 2006, **8**(4), p 264-267
28. J. Gresham, Aluminum Cladding Replacement, Air Force STTR Topic Release #AF06-T023, 2006
29. Tecnar Automation DPV-2000 Reference Manual Rev. 5.0
30. W.S. Rasband, ImageJ, U.S. National Institute of Health, Bethesda, Maryland, USA, http://www.rsb.info.nih.gov/ij, 1997-2006
31. "Standard Test Method for Bending Fatigue Testing for Copper-Alloy Spring Materials," B 593-96, *Annual Book of ASTM Standards*, Vol. 02.01, ASTM
32. "Standard Test Method for Adhesion or Cohesion Strength of Thermal Spray Coatings," C 633-01, *Annual Book of ASTM Standards*, Vol. 02.05, ASTM
33. A.H. Shapiro, *The Dynamics and Thermodynamics of Compressible Fluid Flow*. Ronald Press, New York, 1953
34. B. Jodoin, Cold Spray Nozzle Mach Number Limitation, *J. Thermal Spray Technol.*, 2002, **11**(4), p 496-507
35. J. Mondoux, Development of a Cold-Gas Dynamic Spraying System for Parameter Study of Aluminum Coatings, M. Sc. Thesis, University of Ottawa, 2004
36. T. Van Steenkiste and J.R. Smith, Evaluation of Coatings Produced via Kinetic and Cold Spray Processes, *J. Thermal Spray Technol.*, 2004, **13**(2), p 274-282
37. S. Sampath, X.Y. Jiang, J. Matejicek, L. Prchlik, A. Kulkarni, and A. Vaidya, Role of Thermal Spray Processing Method on the Microstructure, Residual Stress and Properties of Coatings: An Integrated Study for Ni-5 wt.% Al Bond Coats, *Mater. Sci. Eng. A*, 2004, **364**(1-2), p 216-231
38. I. Kraus and N. Ganev, Residual Stress and Stress Gradients, *Industrial Applications of X-Ray Diffraction*, F.H. Chung and D.K. Smith, Ed., Marcel Dekker Inc., New York, 2000
39. R. Jenkins and R.L. Snyder, Introduction to X-ray Powder Diffractometry. John Wiley & Sons, New York, 1996